OEA | Opto-Electronic Advances

In-situ and ex-situ twisted bilayer liquid crystal computing platform for reconfigurable image processing

Kang Zeng†, Yougang Ke†*, Zhangming Hong, Linzhou Zeng* and Xinxing Zhou*

https://doi.org/10.29026/oea.2025.250226

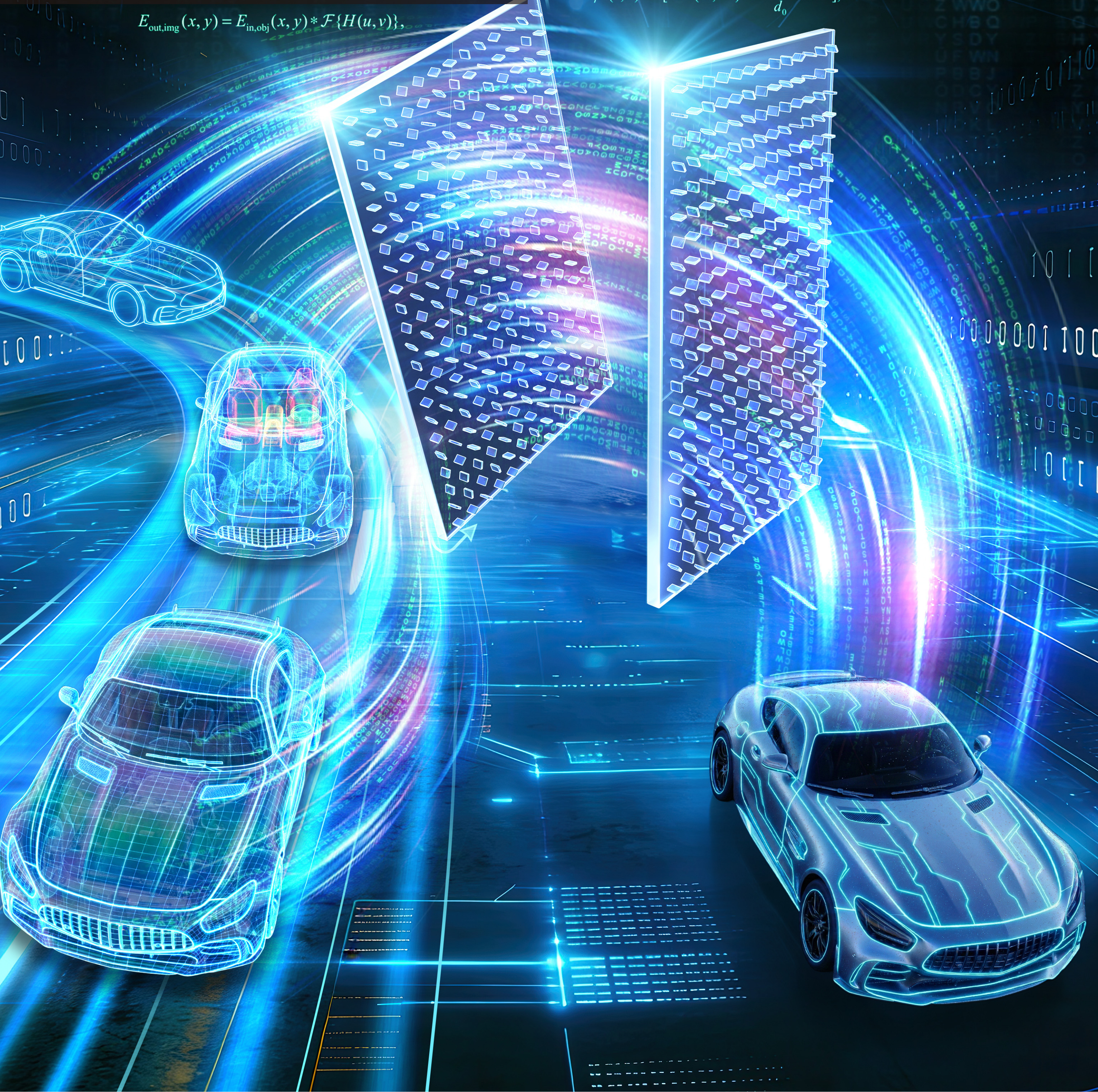

Opto-Electronic Advances

CN 51–1781/TN ISSN 2096–4579 (Print) ISSN 2097–3993 (Online)

In-situ and ex-situ twisted bilayer liquid crystal computing platform for reconfigurable image processing

Kang Zeng, Yougang Ke, Zhangming Hong, Linzhou Zeng and Xinxing Zhou

Citation: Zeng K, Ke YG, Hong ZM, et al. In-situ and ex-situ twisted bilayer liquid crystal computing platform for reconfigurable image processing. *Opto-Electron Adv* **8**, 250226(2025).

https://doi.org/10.29026/oea.2025.250226

Received: 29 August 2025; Accepted: 16 November 2025; Published online: 25 December 2025

Opto-Electronic Advances

Article

December 2025, Vol. 8, No. 12

DOI: 10.29026/oea.2025.250226 CSTR: 32247.14.oea.2025.250226

In-situ and ex-situ twisted bilayer liquid crystal computing platform for reconfigurable image processing

Kang Zeng[1†], Yougang Ke[1†*], Zhangming Hong[1], Linzhou Zeng[1*] and Xinxing Zhou[2*]

All-optical image processing has been viewed as a promising technique for its high computation speed and low power consumption. However, current methods are often restricted to few functionalities and low reconfigurabilities, which cannot meet the growing demand for device integration and scenario adaptation in next-generation vision regimes. Here, we propose and experimentally demonstrate a bilayer liquid crystal computing platform for reconfigurable image processing. Under different in-situ/ex-situ twisted/untwisted conditions of the layers, our approach allows for eight kinds of image processing functions, including one/two-channel bright field imaging, one/two-channel vortex filtering, horizontally/vertically one-dimensional edge detection, vertex detection, and photonic spin Hall effect-based resolution adjustable edge detection. A unified theoretical framework for this scheme is established on the transfer function theory, which coincides well with the experimental results. The proposed method offers an easily-switchable multi-functional solution to optical image processing by introducing mechanical degrees of freedom, which may enable emerging applications in computer vision, autonomous driving, and biomedical microscopy.

Keywords: reconfigurable image processing; bilayer liquid crystal; mechanical operation; photonic spin Hall effect

Zeng K, Ke YG, Hong ZM et al. In-situ and ex-situ twisted bilayer liquid crystal computing platform for reconfigurable image processing. *Opto-Electron Adv* **8**, 250226 (2025).

Introduction

Image processing refers to a set of techniques for manipulating, enhancing, and analyzing images, which has found applications in various fields such as photography, robotics, and medicine[1,2]. Conventional image processing relies on the use of a digital electronic computer to perform designated algorithms on pixelated images. With the increasing requirement for computation speed and energy efficiency, optical analog computing has emerged as a promising alternative by leveraging the high speed and inherent parallelism of light[3–6]. Such systems can directly process physical images formed by the light waves from an object, offering potential for real-time, energy-efficient processing of image data[7–10]. Prominent operations in all-optical image processing include spatial differentiation[11–13], convolution[14] and

[1]School of Information Science and Engineering, Hunan Institute of Science and Technology, Yueyang 414006, China; [2]Key Laboratory of Low-Dimensional Quantum Structures and Quantum Control of Ministry of Education, School of Physics and Electronics, Hunan Normal University, Changsha 410081, China.

†These authors contributed equally to this work.

*Correspondence: YG Ke, E-mail: yougangke@hnu.edu.cn; LZ Zeng, linzhou.zeng@hnist.edu.cn; XX Zhou, E-mail: xinxingzhou@hunnu.edu.cn

Received: 29 August 2025; Accepted: 16 November 2025; Published online: 25 December 2025

integration[15], indicating its value in real-world applications. Unfortunately, traditional optical image processing platforms consist of bulky components, which compromises portability, integrability, and stability of the system.

Recently, the rapid advancement of nanophotonic materials has provided an effective way to address these issues. Metasurfaces[16–21], two-dimensional materials composed of subwavelength structures[22,23], possess extraordinary capability to control the phase, amplitude, polarization of the light. Particularly, those for computational purposes, a.k.a. computing metasurfaces[24,25], enable mathematical operations on the input optical field, creating opportunities for thin, lightweight optical image processors. However, most planar optical elements offer limited functionality, typically performing only a single operation such as one-dimensional or two-dimensional differentiation. To expand their capabilities or enable resolution switching, existing approaches often rely on complex optical setups or the replacement of different metasurfaces. While these methods can partially enhance system functionality, they still face challenges such as limited reconfigurability, bulky system architectures, and high costs. To introduce dynamic tuning capabilities, researchers have integrated active media[26,27] such as phase-change materials into metasurface structures[28,29]. However, these active configurations often involve complex fabrication processes and higher costs. For instance, devices based on phase-change materials typically rely on thermal stimuli for state switching, which complicates system integration and portability while adding extra cost and power overhead.

Notably, recent advances in liquid crystal (LC)-plasmonic hybrid systems have opened promising pathways toward high-performance tunable optics. For example, Franklin et al. demonstrated a reflective surface capable of full RGB colour tuning via a single nanostructure, leveraging a hybrid mechanism combining bulk and interfacial LC effects[30]. In a follow-up work, the same group achieved a remarkable 95 nm plasmonic resonance shift in the visible spectrum using highly birefringent LCs and optimized nanowells, enabling millisecond-scale switching and full visible-range colour control[31]. These works highlight the potential of LC-integrated platforms in achieving wide-range, fast, and practical reconfigurability[32–35].

Inspired in part by these dynamic tuning concepts, attention has also turned to alternative methods that cascade multiple entirely passive elements[36–41]. This approach enables functional reconfiguration simply by adjusting the relative positions or rotation angles of these elements, offering a compact, integrable, and flexible solution that can be readily embedded into various optical systems. The system also exhibits excellent scalability. By carefully designing the phase profiles, additional LC elements can be integrated to further extend its functional versatility. Although mechanical adjustment is slightly slower than fully electrical control schemes, it significantly reduces system fabrication complexity, power consumption, and cost, thereby presenting a highly promising route for constructing low-cost, multifunctional, and reconfigurable optical systems.

In this paper, we propose and experimentally demonstrate a simple yet effective computing platform based on bilayer LC for reconfigurable image processing. By twisting the layer(s) at in-situ and ex-situ positions, the output beam mode exhibits a series of variations, which enables a range of functions such as bright-field imaging and edge-enhanced imaging. The schematic of the proposed scheme is illustrated in Fig. 1, where the two layers of LC are named as LC_1 and LC_2, respectively. The in-situ position is defined by the perfect alignment of the centers of the two layers, as illustrated in Fig. 1(a). By rotating LC_2 to different angles, one- or two-channel Gaussian and Hermite-Gaussian (HG) beams can be generated, corresponding respectively to the configurations at 0°, 180°, 90°, and 270° in Fig. 1(a). Specifically, the HG beams shown in Fig. 1(a) operate in the HG_{11} mode. Figure 1(b) illustrates the ex-situ position, which occurs when LC_1 and/or LC_2 are displaced from their original locations. When only LC_2 is shifted leftward (with LC_1 stationary), rotating LC_2 to 0° and 180° produces a one vector vortex and two scalar vortices, respectively. Simultaneously shifting both LC_1 and LC_2 leftward or upward, by a displacement of 2.4 mm in all cases, and rotating LC_2 to 90° or 270° yields HG_{01} or HG_{10} modes. Based on the structured beams generated in Fig. 1(a) and 1(b), multiple imaging functionalities can be achieved and switched accordingly, as demonstrated in Fig. 1(c) and 1(d). Notably, each beam pattern at a given angle corresponds to the image processing result at the same angle: patterns in Fig. 1(a) match results in Fig. 1(c), and those in Fig. 1(b) correspond to results in Fig. 1(d). Such a reconfigurable image processor simultaneously features low expense, high compactness, and wide applicability, which may advance the field of optical analog computing.

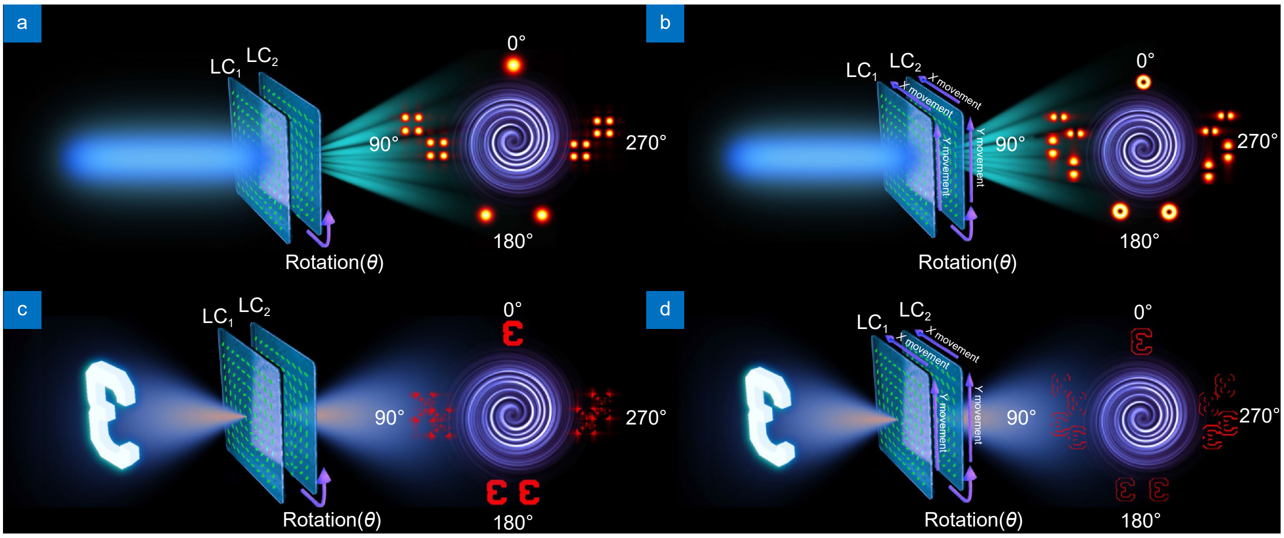

Fig. 1 | Schematic diagram of the proposed scheme. (**a**) Intensity patterns obtained by rotating LC_2 at the in-situ position. (**b**) Intensity patterns obtained by rotating LC_2 at the ex-situ position. (**c**) Bright-field imaging and vertex detection functionality corresponding to (a), where the single Gaussian spot pattern at 0° in (a) corresponds to the single bright-field image processing result at 0° in (c), and the same correspondence applies to the remaining patterns. (**d**) Edge-enhanced imaging functionality corresponding to (b), where the single vortex spot pattern at 0° in (b) corresponds to the single two-dimensional imaging processing result at 0° in (d), with analogous correspondences for the other patterns.

Design and principle

Phase design

Recent years have witnessed remarkable advances in planar optics based on the geometric phase, particularly through LC materials. As a state of matter intermediate between isotropic liquids and crystalline solids, LCs combine fluidity with anisotropic optical properties. Their molecules tend to align along a preferred direction, described by the local director, which defines the optical axis and enables spatially varying birefringence. More importantly, LCs exhibit a number of advantageous characteristics: high transparency across a broad spectral range, large and tunable birefringence, and responsiveness to external stimuli such as electric fields and surface alignment. These properties make them ideal candidates for reconfigurable metasurfaces and wavefront-shaping elements[42,43].

For optical edge detection, several differentiation schemes have been established, each with distinct strengths and limitations. The photonic spin Hall effect-based (PSHE) approach enables directional edge extraction with tunable edge thickness by varying the grating period; vortex-filtering methods capture full two-dimensional edges; HG modes such as HG_{10}/HG_{01} allow polarization-independent differentiation along one axis, while the HG_{11} mode supports vertex detection by highlighting intersections of x- and y-directional edges.

To leverage these complementary behaviors in a single platform, we aim to develop a unified phase formulation that would allow dynamic switching between differentiation modes. Initial designs relying solely on rotational tuning proved insufficient. While rotation enabled PSHE-type differentiation and HG_{11}-mode vertex detection, it could not access vortex or single-axis HG modes. This motivated the introduction of lateral displacement as an additional control degree. The phase profile on either piece of the LC in the compact bilayer LC system is designed as[40]

$$\varphi^{\pm}(r,\theta)=\pm\left[\text{mod}(l\theta,2\pi)/2+\frac{2\pi}{d_0}r\cos\theta\right],\tag{1}$$

where (r,θ) denotes the polar coordinates, the symbol "+" or "−" corresponds to left-handed circularly polarized (LCP) or right-handed circularly polarized (RCP) incident light, respectively. In this work, we set $l=2$ and $d_0=0.432$ mm.

In the Cartesian coordinate system, we can derive the total phase at in-situ and ex-situ positions under twist as[40]

$$\begin{aligned}\varphi^{\pm}_{\text{bilayer}}(x,y)\\ =&\pm\varphi_1((x-x_1)\cos\theta_1-(y-y_1)\sin\theta_1,\\ &(x-x_1)\sin\theta_1+(y-y_1)\cos\theta_1)\\ &\mp\varphi_2((x-x_2)\cos\theta_2-(y-y_2)\sin\theta_2,\\ &(x-x_2)\sin\theta_2+(y-y_2)\cos\theta_2)\\ =&\pm\bmod\left(l\cdot\arctan\frac{(x-x_1)\sin\theta_1+(y-y_1)\cos\theta_1}{(x-x_1)\cos\theta_1-(y-y_1)\sin\theta_1},2\pi\right)/2\\ &\pm\frac{2\pi}{d_0}((x-x_1)\cos\theta_1-(y-y_1)\sin\theta_1)\\ &\mp\bmod\left(l\cdot\arctan\frac{(x-x_2)\sin\theta_2+(y-y_2)\cos\theta_2}{(x-x_2)\cos\theta_2-(y-y_2)\sin\theta_2},2\pi\right)/2\\ &\mp\frac{2\pi}{d_0}((x-x_2)\cos\theta_2-(y-y_2)\sin\theta_2)\,,\end{aligned}\tag{2}$$

where LC_1 and LC_2 are translated by (x_1, y_1) and (x_2, y_2) along the x- and y-axes, respectively, and subsequently rotated by θ_1 and θ_2 around their respective centers. Here, both LC_1 and LC_2 share the same phase function as in Eq. (1). To distinguish between them, $\varphi_1(r,\theta)$ is used to denote the phase of LC_1, while $\varphi_2(r,\theta)$ denotes that of LC_2.

Unified transfer function

In the $4f$ system, denote the final illuminated object of the incident electric field by $E_{\text{in,obj}}(x,y)$. Then, the relationship between the input and output fields can be expressed as

$$E_{\text{out,img}}(x,y)=E_{\text{in,obj}}(x,y)*\mathrm{F}\{H(u,v)\},\tag{3}$$

where $u=x'/\lambda f$ and $v=y'/\lambda f$. Note that position coordinates (x',y') at the Fourier plane, corresponding to spatial frequencies $(u,v)=(x'/\lambda f, y'/\lambda f)$, F denotes the Fourier transform, and the symbol $*$ represents the convolution operation. Notably, $H(u,v)$ represents the transfer function in the Fourier plane, as given by

$$\begin{aligned}H^{\pm}(u,v)=&\exp\left[\pm\mathrm{i}\cdot\bmod\left(l\cdot\arctan\frac{(u-u_1)\sin\theta_1+(v-v_1)\cos\theta_1}{(u-u_1)\cos\theta_1-(v-v_1)\sin\theta_1},2\pi\right)/2\pm\mathrm{i}\cdot\frac{2\pi}{d_0}((u-u_1)\cos\theta_1-(v-v_1)\sin\theta_1)\right.\\ &\left.\mp\mathrm{i}\cdot\bmod\left(l\cdot\arctan\frac{(u-u_2)\sin\theta_2+(v-v_2)\cos\theta_2}{(u-u_2)\cos\theta_2-(v-v_2)\sin\theta_2},2\pi\right)/2\mp\mathrm{i}\cdot\frac{2\pi}{d_0}((u-u_2)\cos\theta_2-(v-v_2)\sin\theta_2)\right],\end{aligned}\tag{4}$$

which allows for various functions by altering the parameters u_1, v_1, u_2, v_2, θ_1, and θ_2. In the system, the center of each LC layer is typically aligned with the optical axis, which corresponds to the origin of the Cartesian coordinate system. Accordingly, u_1 and u_2 denote the translational displacements of LC_1 and LC_2 along the x-axis, v_1 and v_2 represent their translations along the y-axis, while θ_1 and θ_2 are the rotation angles of LC_1 and LC_2 about their own centers, respectively. In the following, we show how those functionalities are obtained under different parameter settings.

One/two-channel bright-field imaging

The one- and two-channel bright-field imaging can be obtained by rotating LC_2 by 0° and 180°, respectively, in the absence of any spatial displacement (i.e., the in-situ case).

For the one-channel bright field imaging, the parameter conditions are set as $u_1=0$, $v_1=0$, $u_2=0$, $v_2=0$, $\theta_1=0°$, and $\theta_2=0°$. Substituting these conditions into Eq. (4), we have

$$H^{0°}_{\text{o-bright}}(u,v)=\exp(0).\tag{5}$$

This shows that the transfer function applied to the incident field is unity. Hence, the corresponding expression for the one-channel bright field imaging can be obtained as

$$\begin{aligned}E_{\text{out,o-bright}}(x,y)&=E_{\text{in,obj}}(x,y)*\mathrm{F}\left\{H^{0°}_{\text{o-bright}}(u,v)\right\}\\ &=E_{\text{in,obj}}(x,y).\end{aligned}\tag{6}$$

In contrast, the two-channel bright field imaging can be realized under $u_1=0$, $v_1=0$, $u_2=0$, $v_2=0$, $\theta_1=0°$ and $\theta_2=180°$. From Eq. (4), the transfer function now becomes

$$H^{180°}_{\text{d-bright}}(u,v)=\exp\left(\pm\mathrm{i}\cdot\frac{4\pi}{d_0}u\right).\tag{7}$$

This leads to a one-dimensional grating modulation within the $4f$ system. Accordingly, under linear polarization, the two-channel bright field imaging can be expressed as[44,45]

$$\begin{aligned}E_{\text{out,d-bright}}(x,y)=&E_{\text{in,obj}}(x,y)*\mathrm{F}\left\{H^{180°}_{\text{d-bright}}(u,v)\right\}\\ =&E_{\text{in,obj}}[(x-\Delta),y]\begin{bmatrix}1\\-\mathrm{i}\end{bmatrix}\\ &+E_{\text{in,obj}}[(x+\Delta),y]\begin{bmatrix}1\\\mathrm{i}\end{bmatrix},\end{aligned}\tag{8}$$

where $\begin{bmatrix}1 & \pm\mathrm{i}\end{bmatrix}^{\mathrm{T}}/\sqrt{2}$ denote the LCP and RCP components, respectively, and Δ represents the spatial displacement. For this function, the displacement is sufficiently large to form two spatially separated bright-field replicas of the object.

Vertex detection

In the in-situ case, vertex detection can be implemented within the 4f system based on the generated HG_{11} mode via rotating solely LC_2 by 90°. At this point, the parameter conditions are set as $u_1 = 0$, $v_1 = 0$, $u_2 = 0$, $v_2 = 0$, $\theta_1 = 0°$ and $\theta_2 = 90°$. The resulting transfer function can be written as

$$H^{90°}_{HG_{11}}(u,v)=\exp\left[\pm i\left[V(u,v)-V(-v,u)+\frac{2\pi}{d_0}(u+v)\right]\right], \tag{9}$$

where the function $V(u,v)$ is defined as $\pm\text{mod}\left(2\arctan\frac{v}{u},2\pi\right)/2$. The linear term $L=\frac{2\pi}{d_0}(u+v)$ only affects the spatial location of the differentiation result, which does not alter the differentiation process.

Considering the property of the mod function in the first quadrant, rewrite

$$H^{90°}_{HG_{11}}(u,v)=\exp\left[\pm i\left[\left(\arctan\frac{v}{u}-\arctan\frac{-u}{v}\right)+\frac{2\pi}{d_0}(u+v)\right]\right], \tag{10}$$

where the argument without the linear term can be simplified, using trigonometric identities, into

$$\arctan\frac{v}{u}-\arctan\frac{-u}{v}\approx\arctan\left(\frac{\frac{v}{u}+\frac{u}{v}}{1+\frac{v}{u}\cdot\frac{-u}{v}}\right)=\begin{cases}-\frac{\pi}{2}, & uv>0\\ \frac{\pi}{2}, & uv<0\end{cases}. \tag{11}$$

It is easy to show that $\exp\left[\pm i\left(\arctan\frac{v}{u}-\arctan\frac{-u}{v}\right)\right]\sim\exp\left[\pm i\left(\text{sgn}(u)\,\text{sgn}(v)\frac{\pi}{2}\right)\right]$, which is actually a four-quadrant sign function for the HG_{11} mode. The linear term, acting as a grating function, manifests itself as a spatial shift of the image after Fourier transformation. Then, under linear polarization, the output field of the HG_{11} mode can be expressed as

$$\begin{aligned}E_{out,HG_{11}}(x,y)&=E_{in,obj}(x,y)*\mathrm{F}\left\{H^{90°}_{HG_{11}}(u,v)\right\}\\&\propto H_xH_y\left[E_{in,obj}(x-\Delta,y-\Delta)\right.\\&\left.+(x+\Delta,y+\Delta)\right]\end{aligned}, \tag{12}$$

where H_x and H_y represent the Hilbert transform operators in the x- and y-directions, respectively.

Horizontally/vertically oriented one-dimensional edge detection

To achieve horizontally/vertically oriented one-dimensional edge detection, we need to shift both LC_1 and LC_2 vertically/horizontally by 2.4 mm simultaneously (ex-situ case) and then rotate LC_2 by 90°. It is also feasible to rotate LC_2 by 270°, which shares the same principle and thus we focus on the rotation of 90°.

For vertically oriented one-dimensional edge imaging, we use $u_1 = 2.4$ mm, $v_1 = 0$, $u_2 = 2.4$ mm, $v_2 = 0$, $\theta_1 = 0°$, and $\theta_2 = 90°$. This leads to the HG_{01} mode, and the corresponding transfer function can be written as

$$\begin{aligned}H^{90°}_{HG_{01}}(u,v)=\exp\Big[\pm i\Big[&V(u-u_1,v)-V(-v,u-u_1)\\&+\frac{2\pi}{d_0}(u+v-u_1)\Big]\Big],\end{aligned} \tag{13}$$

where $V(u,v)$, as defined before, is $\pm\text{mod}\left(2\arctan\frac{v}{u},2\pi\right)/2$. The HG_{01} mode can be regarded as the HG_{11} mode shifted along the x-axis, resulting in a pattern where the upper and lower regions exhibit a phase difference of π. Then, according to Eq. (12), the output field under linear polarization incidence is given by

$$\begin{aligned}E_{out,HG_{01}}(x,y)&=E_{in,obj}(x,y)*\mathrm{F}\left\{H^{90°}_{HG_{01}}(u,v)\right\}\\&\propto\frac{\partial}{\partial y}\left(E_{in,obj}(x-\Delta,y-\Delta)\right.\\&\left.+E_{in,obj}(x+\Delta,y+\Delta)\right).\end{aligned} \tag{14}$$

For horizontally oriented one-dimensional edge detection, the parameter configuration is $u_1 = 0$, $v_1 = 2.4$ mm, $u_2 = 0$, $v_2 = 2.4$ mm, $\theta_1 = 0°$, and $\theta_2 = 90°$. Similarly, the expression for the HG_{10} mode can be derived as

$$\begin{aligned}E_{out,HG_{10}}(x,y)&=E_{in,obj}(x,y)*\mathrm{F}\left\{H^{90°}_{HG_{10}}(u,v)\right\}\\&\propto\frac{\partial}{\partial x}\left(E_{in,obj}(x-\Delta,y-\Delta)\right.\\&\left.+E_{in,obj}(x+\Delta,y+\Delta)\right).\end{aligned} \tag{15}$$

Resolution-variable one-dimensional edge detection

Resolution-variable one-dimensional edge detection is based on the PSHE. The tunability of this effect is controlled by a small rotation (between −22° and 22°, excluding 0°) of the LC layers. The in-situ bilayer phase becomes

$$\varphi_1(x,y)-\varphi_2(x,y)=\frac{2\pi}{d_0}\left(x\cos\theta_1+y\sin\theta_1\right)-\frac{2\pi}{d_0}\left(x\cos\theta_2+y\sin\theta_2\right). \quad (16)$$

This phase is actually a one-dimensional grating. In particular, for $\theta_1=0$, Eq. (16) can be simplified into

$$G_{\text{bilayer}}=\frac{2\pi}{d_0}\left(x\left(1-\cos\theta_2\right)-y\sin\theta_2\right)=\frac{4\pi}{d_0}\sin\frac{\theta_2}{2}\left[x\sin\frac{\theta_2}{2}-y\cos\frac{\theta_2}{2}\right]. \quad (17)$$

Recall a standard grating with a fixed period d_0 and an arbitrary optical axis direction θ_g, which can be expressed as

$$G_{\text{grating}}=\frac{2\pi}{d_0}(x\cos\theta_g+y\sin\theta_g). \quad (18)$$

Then, compared to the standard grating formula, ours can be simplified toward the standard grating formula, and its period and optical axis direction can be expressed as

$$\theta_{\text{bilayer}}=\arctan\left(\frac{-\sin\theta_2}{1-\cos\theta_2}\right),\quad d_{\text{bilayer}}=\frac{d_0}{2\left|\sin\left(\frac{\theta_2}{2}\right)\right|}. \quad (19)$$

This clearly shows that the grating period as well as the direction of the optical axis changes over rotation. For orthogonal polarization illuminance, if the displacement $\Delta=\frac{\lambda f}{d_{\text{bilayer}}}$ is sufficiently smaller than the image size, the output electric field can be derived as[44,45]

$$E_{\text{out,tunable}}(x,y)=\{E_{\text{in,obj}}\left[x+\Delta\sin\theta_{bilayer},y+\Delta\cos\theta_{\text{bilayer}}\right]-E_{\text{in, obj}}\left[x-\Delta\sin\theta_{\text{bilayer}},y-\Delta\cos\theta_{\text{bilayer}}\right]\}\begin{bmatrix}0\\ \mathrm{i}\end{bmatrix}, \quad (20)$$

where λ is the wavelength and f is the focal length. Considering the amplitude of the output electric field, the output field amplitude becomes approximately proportional to the first-order spatial derivative of the input field, as given by

$$\left|E_{\text{out,edge}}\right|\simeq2\Delta\left|\sin\theta_{\text{bilayer}}\frac{\partial E_{\text{in,obj}}}{\partial x}+\cos\theta_{\text{bilayer}}\frac{\partial E_{\text{in,obj}}}{\partial y}\right|. \quad (21)$$

Therefore, under linear polarization, the output field of the tunable one-dimensional differentiation can be written as

$$E_{\text{out,tunable}}(x,y)=4\frac{\lambda f\left|\sin\frac{\theta_2}{2}\right|}{d_0}\left(\sin\theta_{\text{bilayer}}\frac{\partial E_{\text{in,obj}}}{\partial x}+\cos\theta_{\text{bilayer}}\frac{\partial E_{\text{in,obj}}}{\partial y}\right). \quad (22)$$

The coefficient before the derivative term, which quantifies the resolution, namely the thickness of the edges and the direction of the differentiation, can be adjusted by the rotation angle θ_2.

One-channel vectorial two-dimensional differentiation and two-channel scalar differentiation

One-channel vectorial two-dimensional differentiation is obtained under $u_1=0$, $v_1=0$, $u_2=2.4$ mm, $v_2=0$, $\theta_1=0°$ and $\theta_2=0°$. Again from Eq. (4), the transfer function can now be written as

$$H^{0°}_{\text{o-vortex}}(u,v)=\exp\left[\pm\mathrm{i}\left[V(u,v)-V\left(u-u_2,v\right)+\frac{2\pi}{d_0}\left(u_2\right)\right]\right]. \quad (23)$$

In the expression of $V(u,v)$, it can be seen that $\mathrm{mod}\left(2\arctan\left(\frac{v}{u}\right),2\pi\right)=2\arctan\left(\frac{v}{u}\right)-2\pi\cdot\left\lfloor\frac{2\arctan\left(\frac{v}{u}\right)}{2\pi}\right\rfloor$. Since $\arctan\left(\frac{v}{u}\right)$ belongs to $\left(-\frac{\pi}{2},\frac{\pi}{2}\right)$, we have $\mathrm{mod}\left(2\arctan\left(\frac{v}{u}\right),2\pi\right)=2\arctan\left(\frac{v}{u}\right)$. Similarly, we can obtain that $\mathrm{mod}\left(2\arctan\left(\frac{v}{u-u_2}\right),2\pi\right)=2\arctan\left(\frac{v}{u-u_2}\right)$. Using these results, the transfer function can be simplified as

$$H^{0°}_{\text{o-vortex}}(u,v)=\exp\left[\pm\mathrm{i}\left[\arctan\left(\frac{-u_2v}{u^2-u_2u+v^2}\right)+\frac{2\pi}{d_0}\left(u_2\right)\right]\right]. \quad (24)$$

Consider a small region around the origin, defined by $u=\rho\cos\phi$, $v=\rho\sin\phi(\rho\to0)$, where (ρ,ϕ) denotes the polar coordinates in the LC (Fourier) plane. Rewrite the transfer function as

$$H^{0^\circ}_{\text{o-vortex}}(u,v)\approx \exp\left[\pm\mathrm{i}\left[\arctan\left(\frac{-u_2\rho\sin\phi}{\rho\cos\phi^2-u_2\rho\cos\phi+\rho\sin\phi^2}\right)+\frac{2\pi}{d_0}u_2\right]\right]$$
$$=\exp\left[\pm\mathrm{i}\left[\arctan(\tan\phi)+\frac{2\pi}{d_0}(u_2)\right]\right]$$
$$=\exp\left[\pm\mathrm{i}\left[\phi+\frac{2\pi}{d_0}u_2\right]\right]\ , \tag{25}$$

where $\frac{2\pi}{d_0}u_2$ is a constant. Hence, $H^{0^\circ}_{\text{o-vortex}}(u,v)$ can be approximately regarded as a vector vortex transfer function with the topological charge of 1. Under linear polarization, the output field is given by[46]

$$E_{\text{out,o-vortex}}(x,y)=E_{\text{in,obj}}(x,y)*\mathrm{F}\left\{H^{0^\circ}_{\text{o-vortex}}(u,v)\right\}$$
$$=E_{\text{in,obj}}(x,y)*h(r,\theta)$$
$$=E_{\text{in,obj}}(x,y)*\frac{2\pi}{\lambda f}\begin{bmatrix}\cos(\theta-\theta_{\text{in}})\\ \sin(\theta-\theta_{\text{in}})\end{bmatrix}\cdot\int_0^R \mathrm{J}_1\left(\frac{2\pi}{\lambda f}r\rho\right)\rho\mathrm{d}\rho\ , \tag{26}$$

where (r,θ) denote the polar coordinates in the image plane. In this case, the resulting output corresponds to two-dimensional edge features, realized through a convolution operation.

Two-channel scalar differentiation requires the parameter conditions $u_1=0$, $v_1=0$, $u_2=2.4$ mm, $v_2=0$, $\theta_1=0^\circ$ and $\theta_2=180^\circ$. The transfer function now becomes

$$H^{180^\circ}_{\text{t-vortex}}(u,v)=\exp\left[\pm\mathrm{i}\left[V(u,v)-V(u-u_2,v)+\frac{2\pi}{d_0}(2u-u_2)\right]\right], \tag{27}$$

which, following a similar procedure to Eq. (25), can be reduced into

$$H^{180^\circ}_{\text{t-vortex}}(u,v)=\exp\left[\pm\mathrm{i}\left[\phi+\frac{2\pi}{d_0}(2u-u_2)\right]\right]. \tag{28}$$

Compared with Eq. (25), the only difference here is the linear term $4u\pi/d_0$ instead of the constant. As stated, such a linear term acts as a one-dimensional grating, which would split the vector vortex into LCP and RCP components, i.e., two different channels. By considering the two components separately, the output light field can be expressed as

$$E_{\text{out,t-vortex}}(x,y)=E_{\text{in,obj}}(x,y)*\mathrm{F}\left\{H^{180^\circ}_{\text{t-vortex}}(u,v)\right\}$$
$$=E_{\text{in,obj}}(x-\Delta,y)*\frac{2\pi}{\lambda f}\begin{bmatrix}1\\-\mathrm{i}\end{bmatrix}\cdot H^{180^\circ}_{\text{t-vortex-lcp}}(u,v)\int_0^R \mathrm{J}_1\left(\frac{2\pi}{\lambda f}r\rho\right)\rho\mathrm{d}\rho$$
$$+E_{\text{in,obj}}(x+\Delta,y)*\frac{2\pi}{\lambda f}\begin{bmatrix}1\\ \mathrm{i}\end{bmatrix}\cdot H^{180^\circ}_{\text{t-vortex-rcp}}(u,v)\int_0^R \mathrm{J}_1\left(\frac{2\pi}{\lambda f}r\rho\right)\rho\mathrm{d}\rho. \tag{29}$$

Results and discussion

Structured light generation

According to the designed phase function, two LC samples, i.e., LC_1 and LC_2, were fabricated, as presented in Fig. 2(a). To verify the optical properties of the samples, cross-polarized imaging was performed on LC_1, while parallel and cross-polarized images were captured for LC_2. The central region of the cross-polarized image for LC_2 was magnified to examine its structural details, which was fork-shaped. Comparing the parallel/cross-polarized images with the designed phase distributions, we can confirm that the fabricated samples exhibit spatial phase modulation characteristics that are highly consistent with the theoretical design. The LC phase elements were fabricated via laser direct writing[47]. The fabrication procedure is outlined as follows: First, a transparent glass substrate was thoroughly cleaned. Then, a solution of sulphonic azo-dye (SD1) was applied to form an alignment layer on the substrate. Subsequently, the designed phase pattern was transferred onto the substrate point-by-point using a laser direct writing system. Following this, the substrate was spin-coated with a LC monomer solution to form a polymer network. Finally, the sample was exposed to ultraviolet light to solidify the LC alignments. The resulting LC pattern consists of 1080×1080 pixels with a single-pixel size of 8 μm. Characterization measurements confirm that both LC_1 and LC_2 exhibit a transmittance greater than 98% at the design wavelength of 633 nm. Furthermore, the deviation of their measured retardance from the ideal half-wave plate value is merely 0.76% for LC_1 and 0.83% for LC_2. These parameters demonstrate that the fabricated elements closely match the theoretical design specifications.

To test the LC elements, an experimental setup is established, as depicted in Fig. 2(b). A He-Ne laser (Thorlabs) is utilized to emit a linearly polarized Gaussian beam at the wavelength of 632.8 nm. Its intensity can be controlled by a half-wave plate (HWP) and a Glan laser polarizer (GLP_1). Meanwhile, the combination of GLP_1 and a quarter-wave plate (QWP_1) enables precise control of the incident light polarization state. After the polarization modulation, the beam illuminates the central region of the LC layer. The two LC layers are kept as closely adjacent as possible. Specifically, during all experimental procedures, the distance separating the two LC layers is ensured to be within 10 mm. Although a slight gap inevitably exists between the two LC layers, its influence on the generation of the expected phase profile is negligible. Subsequently, the Stokes parameter S_3 of the output optical field is analyzed using QWP_2 and GLP_2. Finally, the output intensity can be recorded by a CCD camera. In the experiment, we first construct various structured light fields under linear polarization incidence by twisting LC_2 at in-situ position, as shown in Fig. 2(c). When the twist angle of LC_2 is 0°, the phase profiles of the two LC layers are identical, canceling each other out and resulting in an overall composite phase of zero. Consequently, the output remains the form of a single Gaussian spot. When the rotation angles of LC_2 are 90° and 270°, the composite phase modulation corresponds to HG_{11} mode, only differing in direction. If LC_2 is rotated to 180°, the composite phase of LC_1 and LC_2 forms a one-dimensional grating structure, splitting the far-field intensity into two circular spots. The experimental intensity images in the fifth column of Fig. 2(c) show excellent agreement with the theoretical results in the fourth column, validating the correctness and feasibility of the design for the LC layers.

Building upon the in-situ condition in Fig. 2(c), we further consider the ex-situ condition to achieve more diverse beam modes, as depicted in Fig. 3. In the experiment, the geometric centers of the LC layers are defined as the origins, used as the reference for determining offset direction and distance. When the rotation angle of LC_2 is 0°, with LC_2 offset leftward horizontally by 2.4 mm from its origin, we obtain a spot pattern that exhibits single vector vortex characteristics. When the rotation angle of LC_2 is 90° or 270°, shifting both LC_1 and LC_2 leftward by 2.4 mm from their respective origins transforms the spot pattern from the initial HG_{11} mode into the HG_{01} mode. Under the same rotation angles, offsetting both LC_1 and LC_2 upward by 2.4 mm vertically may convert the original HG_{11} mode to the HG_{10} mode. Furthermore, if the rotation angle of LC_2 is 180°,

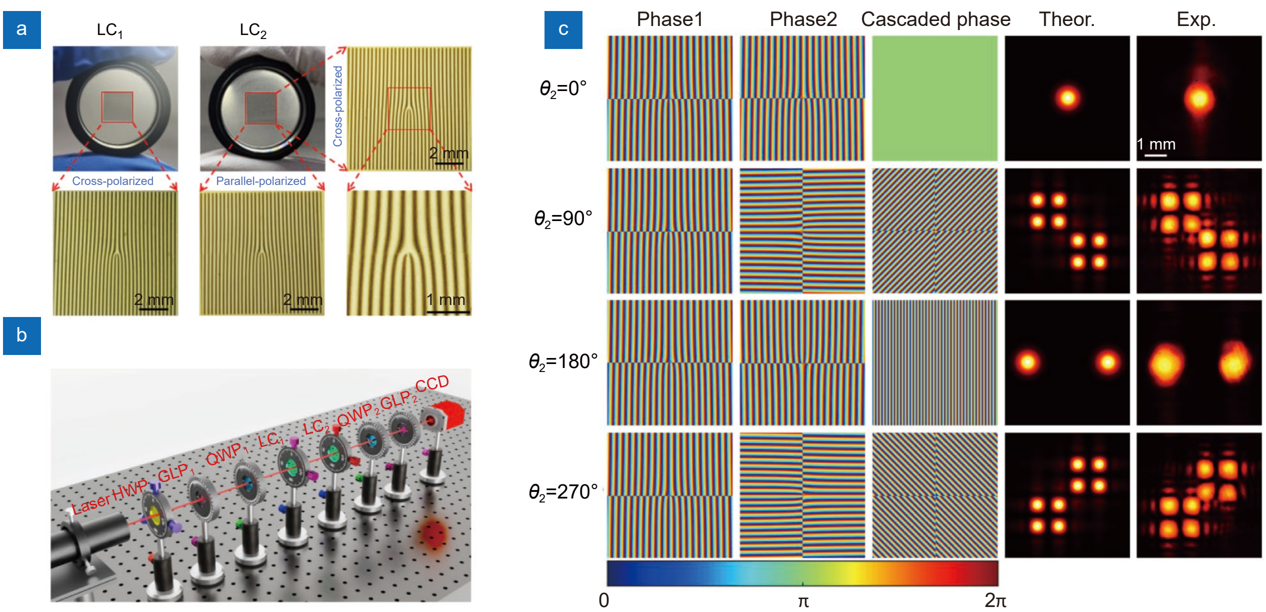

Fig. 2 | LC samples and in-situ beam generation under the twist of LC_2. (**a**) Two fabricated LC elements, LC_1 and LC_2. Cross polarized image for LC_1, parallel and cross polarized images for LC_2. The central region of the cross polarized image for LC_2 is magnified for detail observation. (**b**) Schematic diagram of the experimental setup. (**c**) Phase modulation and corresponding intensity distributions after cascading LC_1 and LC_2. The rotation angle of LC_2 (i.e., Phase2) changes from the first to the fourth row. The first to fifth columns sequentially show the phase distribution of LC_1 (Phase1), the phase distribution of LC_2 (Phase2), the cascaded phase distribution, the theoretical far-field intensity distribution, and the experimental far-field intensity image. Scale bars: 2 mm for the images under crossed or parallel polarizers; 1 mm for the zoomed-in view. Experimental results are displayed under a same scale bar (1 mm).

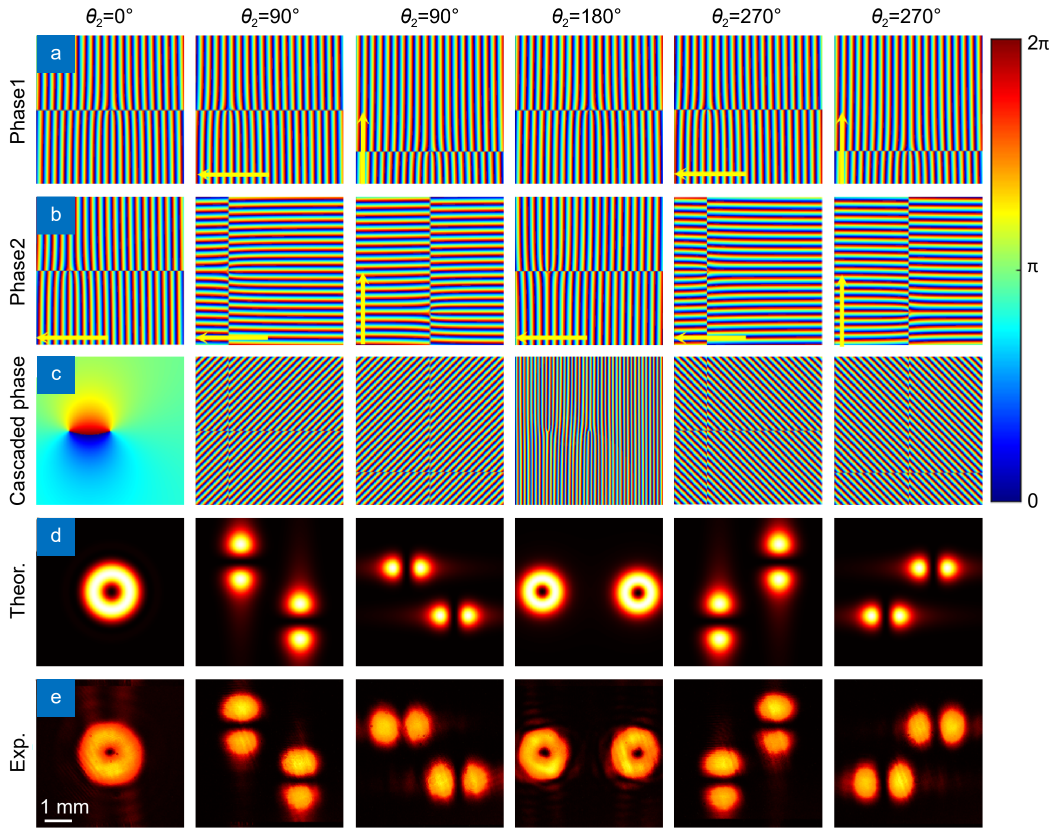

Fig. 3 | Ex-situ beam generation under the twist of LC_2. (**a**) Phase distribution of LC_1 (Phase1). The yellow arrow indicates a 2.4 mm positional offset of LC_1 relative to the beam center. (**b**) Phase distribution of LC_2 (Phase2). (**c**) Composite phase after cascading LC_1 and LC_2. (**d**) Theoretical far-field intensity distributions based on the composite phase. (**e**) Corresponding experimental far-field intensity distributions, with a uniform 1 mm scale bar. Columns from left to right correspond to different rotation angles of LC_2.

offsetting only LC_2 leftward by 2.4 mm yields a two scalar vortex mode. These experimental results demonstrate the effective reconfiguration of various light fields by the synergistic combination of spatial offset and angular control.

Imaging processing demonstration

To utilize the generated structured light fields for image processing, we construct an experimental platform based on a 4*f* system, which is illustrated in Fig. 4(a). In this setup, the laser beam first pass through a HWP and a GLP for intensity and polarization adjustment, before illuminating the target object. Following the target is a 4*f* system that comprises two lenses (L_1 and L_2, with the focal length of 100 mm). The bilayer LC (LC_1 and LC_2) is placed at the confocal plane between L_1 and L_2. For linear polarization control, a linear polarizer P_1 is inserted between L_1 and LC, and another linear polarizer P_2 is placed between LC and L_2. Finally, the output image is captured by a CCD camera. Within this system, various types of imaging effects can be achieved by twisting LC_2 combined with the in-situ/ex-situ positions. Under the in-situ condition, rotating LC_2 to 0° generates the single Gaussian beam, which produces the bright-field image shown in Fig. 4(b). The pattern selected for the experiment is the number '3' from Group 1 of the test target, which has a spatial resolution of 2.52 lp/mm. Based on our measurements, the maximum resolution achievable by the system is 28.5 lp/mm. When LC_2 is rotated to 180°, the dual Gaussian mode results in a two bright-field image, as shown in Fig. 4(c). The two-channel bright-field imaging capability lays the foundation for constructing parallel optoelectronic processing systems, simultaneously meeting the data input requirements for both real-time display and subsequent analysis modules. Figure 4(d) and 4(e) show the experimentally measured results corresponding to Fig. 4(b) and Fig. 4(c), respectively. Rotating LC_2 to 0° while introducing a 2.4 mm spatial displacement generates a vector vortex pattern, leading to a typical two-dimensional edge-enhanced imaging. Its theoretical calculation result is shown in Fig. 4(f). Under orthogonal polarization configurations of P_1

and P_2, the theoretical result in Fig. 4(g) exhibits one-dimensional edge detection characteristics, and also verifies that the vortex is vectorial. Figure 4(h) and 4(i) show the experimentally measured results corresponding to Fig. 4(f) and Fig. 4(g), respectively, which match the theoretical calculations well. Furthermore, rotating LC_2 to 90° and 270° at in-situ position modulates the beam into the HG_{11} mode, which can be used to extract line intersections in the object profiles. Such responses to intersection structures are often called vertex detection. Figure 4(j) shows the relevant theoretical simulation results for it. The first row shows the theoretical edge map under LCP incidence, the second row shows the theoretical result under linear polarization incidence with LC_2 rotated to 90°, and the third and fourth rows show the corresponding simulation images for LC_2 rotated to 270°. Figure 4(k) shows the experimental results corresponding to Fig. 4(j), validating the correctness of the theoretical calculation. It can be seen that vertices are effectively detected by identifying the common intersections of edges in the *x*- and *y*-directions[48]; however, vertices not formed by intersections of edges strictly aligned with the *x*- and *y*-directions yield responses exhibiting a triangular-like structure. Furthermore, experimental measurements reveal that the minimum detectable distance between vertices is about 17.54 μm. In applications requiring object contour extraction, this optical system offers advantages of low energy consumption and high efficiency, as it performs analog computations at the speed of light through parallel propagation, eliminating the need for analog-to-digital conversion.

We further investigate the ex-situ condition with more twist angles of LC_2. For intuitive illustration, a schematic diagram depicting the rotation and spatial displacement of the bilayer LC in the 4*f* system is presented in Fig. 5(a). Figure 5(b–f) clearly show the edge imaging results under the modulation effects of different displacement directions and rotation angles. From left to right, the first column shows the theoretical results under linear polarization incidence. The second and third columns display the theoretical results under LCP and RCP incidence, respectively. The fourth column shows the experimental

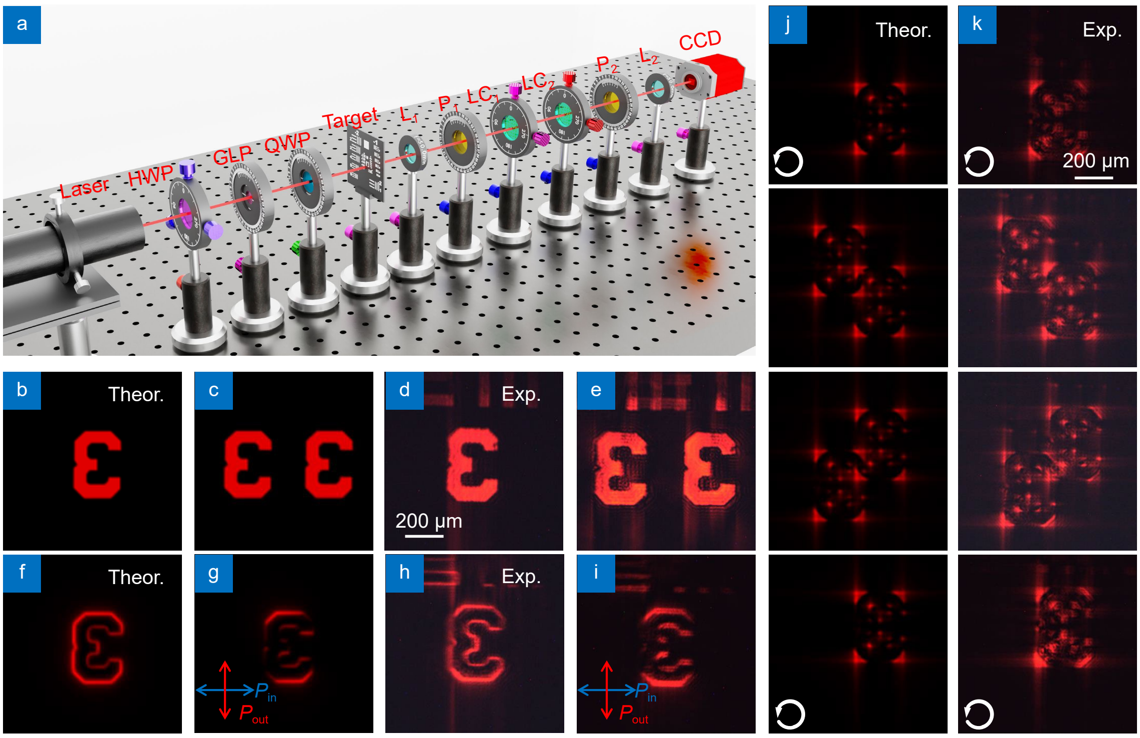

Fig. 4 | Platform and results for image processing at in-situ and ex-situ positions. (**a**) Experimental setup constructed for multifunctional edge detection. (**b**) Theoretical bright-field imaging result corresponding to the single Gaussian mode. (**c**) Theoretical bright-field imaging result corresponding to the dual Gaussian mode. (**d**, **e**) Experimentally measurement corresponding to (b, c), respectively. (**f**) Theoretical two-dimensional edge detection result obtained under vector vortex structured light illumination. (**g**) Theoretical one-dimensional edge detection image for the vector vortex under orthogonal polarization conditions. (**h**, **i**) Experimental measurement corresponding to (f, g), respectively. (**j**) Theoretical edge detection results corresponding to the HG_{11} mode under different incident polarization states (linear and LCP). (**k**) Experimental measurement corresponding to (j). All measured images are displayed with a uniform scale bar (200 μm).

results under linear polarization incidence. The fifth and sixth columns show the experimental results under LCP and RCP illumination, respectively. From up to down in Fig. 5, each row represents the imaging effect under different bilayer configurations detailed in Fig. 5(a). Specifically, when the LC_2 rotation angle is 180° and the LC_2 is offset leftward by 2.4 mm, the generated dual scalar vortex beam results in two side-by-side two-dimensional edge profiles. By adjusting the incident polarization state, two-dimensional edge detection patterns corresponding to single scalar vortices under LCP and RCP conditions can be obtained. When the LC_2 rotation angle is 90° or 270° and both LC_1 and LC_2 are offset leftward by 2.4 mm, the formed HG_{01} mode performs optical differentiation along the *y*-direction, yielding a vertically one-dimensional edge image. Similarly, single-edge responses can be obtained by adjusting the incident polarization state. When the LC_2 rotation angle is 90° or 270° and both LC_1 and LC_2 are offset upward by 2.4 mm, the formed HG_{10} mode conducts differentiation along the *x*-direction. Single-edge extraction can also be achieved by adjusting the incident polarization state. In each row, we can see that the theoretical and experimental results shows good consistency, demonstrating the practical value of this method.

Besides the aforementioned imaging functions by large-angle rotations, resolution-variable one-dimensional edge detection can also be achieved by applying fine-angle rotations to the LC under the single Gaussian mode. This is induced by the PSHE, which makes the phase element, in this case, behave like a one-dimensional tunable grating. To further illustrate the influence of angular variation on the PSHE displacement, representative rotation angles (−4°, −10°, −15°, −20°) are selected, and the corresponding spot splitting trends are plotted in Fig. 6(a). Analysis of the S_3 parameters reveals the spatial separation between LCP (red) and RCP (blue) components, as shown in Fig. 6(b). Figure 6(c) and 6(d) present the experimental results corresponding to Fig. 6(a) and 6(b), respectively, showing excellent agreement. Such tunable spin-dependent splitting in the PSHE can be used to achieve resolution-variable edge imaging. In Fig. 6(e), the theoretical one-dimensional edge detection results show an increase in edge thickness with increasing rotation angle. This trend is well corroborated by the experimental results in Fig. 6(f), further confirming the accuracy of the theoretical model. To more intuitively visualize the change in edge thickness, we plot the intensity distributions of the experimental images in Fig. 6(f) along the white solid lines therein.

To quantitatively analyze the intensity profiles in Fig. 6(g–j), the edge thickness was determined by calculating

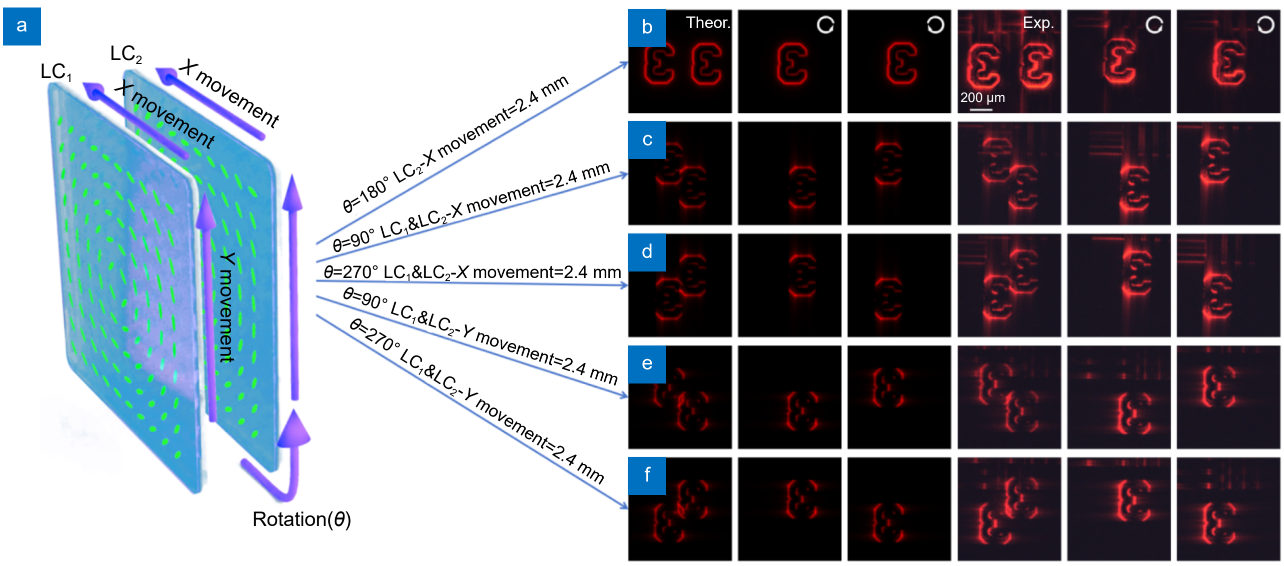

Fig. 5 | Imaging processing at ex-situ position. (**a**) Schematic illustration of the shift and twist configurations of the bilayer LC. (**b**) Comparison of theoretical and experimental edge detection results by dual scalar vortex structured light under LC_2 rotation of 180° and leftward offset of 2.4 mm. (**c**, **d**) Theoretical and experimental edge detection results for the HG_{01} mode obtained when both LC_1 and LC_2 are offset leftward by 2.4 mm under LC_2 rotations of 90° and 270°, respectively. (**e**, **f**) Theoretical and experimental edge detection image comparisons for the HG_{11} mode obtained when both LC_1 and LC_2 are offset upward by 2.4 mm under LC_2 rotations of 90° and 270°, respectively. All experimental images are displayed with a uniform scale bar (200 μm).

the number of pixels between the initial rise and the final decay points on the normalized intensity curve. This pixel count was then converted into a physical length using the known pixel size of 1.85 μm×1.85 μm. The results show that as the spin-dependent displacement increases, the peaks in the intensity curve stretch more, making the edges appear thicker. Subsequently, the actual thicknesses of the edge regions in the intensity images are extracted and analyzed, which gives us the results of 31.45, 57.35, 66.6 and 146.15 μm. For different application scenarios, resolution-tunable edge detection enables a flexible balance between precision and efficiency. For example, high-resolution edge detection is more suitable for applications demanding high accuracy, such as medical imaging and industrial inspection. Conversely, in scenarios with strong real-time requirements like object counting or video surveillance, a lower resolution can enhance processing speed and improve the robustness of feature extraction.

To intuitively analyze the reasons for the resolution decline in Fig. 6(e, f), we compared the synthesized phase generated by the bilayer LC device with the ideal phase calculated using the theoretical grating formula by Eq. (18), as shown in Fig. 7(a) and 7(d). The period and direction of the grating are determined by Eq. (19). When the rotation angles are 4°, 10°, 15°, and 20°, the corresponding grating directions are −88°, −85°, −82.5°, and −80°, and the corresponding grating periods are 6.189 mm, 2.479 mm, 1.655 mm, and 1.244 mm, respectively. The light intensity results derived from the phase distributions in Fig. 7(a) and 7(d) are shown in Fig. 7(b) and 7(e). It can be observed that both exhibit a high degree of consistency in terms of light intensity deviation from the *y*-axis direction and the splitting trend. However, as the rotation angle increases, the optical spot energy generated by the synthesized phase gradually leaks outward, forming interference fringes in the *y*-direction. From the edge detection results, as shown in Fig. 7(c) and 7(f), it is evident that the resolution of the edge pattern generated by the bilayer LC device gradually decreases with increasing rotation angles, whereas the ideal grating phase does not exhibit similar resolution degradation during rotation. The fundamental reason for this discrepancy is that, as the rotation angle increases, the gaps in the

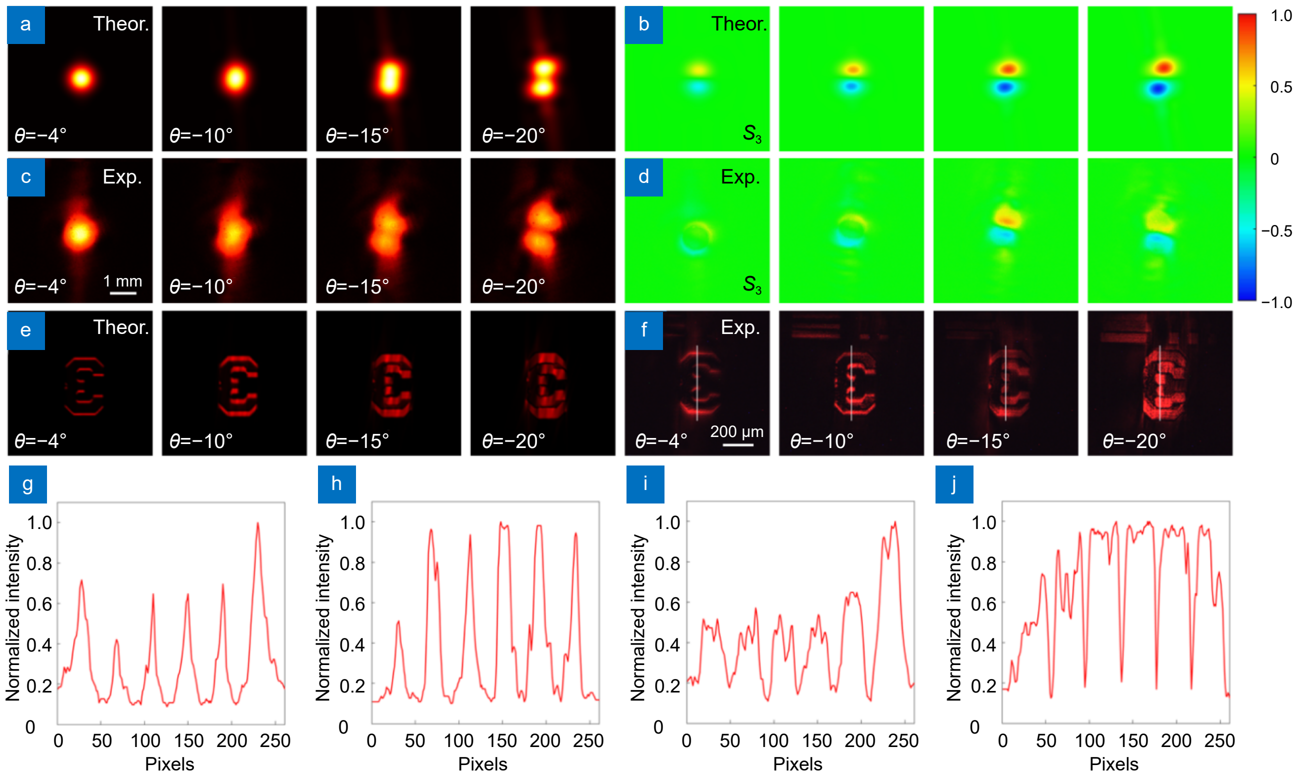

Fig. 6 | Tunable photonic spin Hall effect and the corresponding edge detection results under fine rotation of LC_2. (**a**) Theoretical intensity distributions under fine angular deflection. (**b**) Corresponding theoretical S_3 parameter distributions. (**c**, **d**) Experimental results corresponding to (a) and (b), respectively. sharing a 1 mm scale bar. (**e**) Theoretical edge detection results based on the photonic spin Hall effect. (**f**) Experimental result corresponding to (e), sharing a 200 μm scale bar. (**g–j**) Intensity plots along the white solid lines indicated in the four images from left to right in (f).

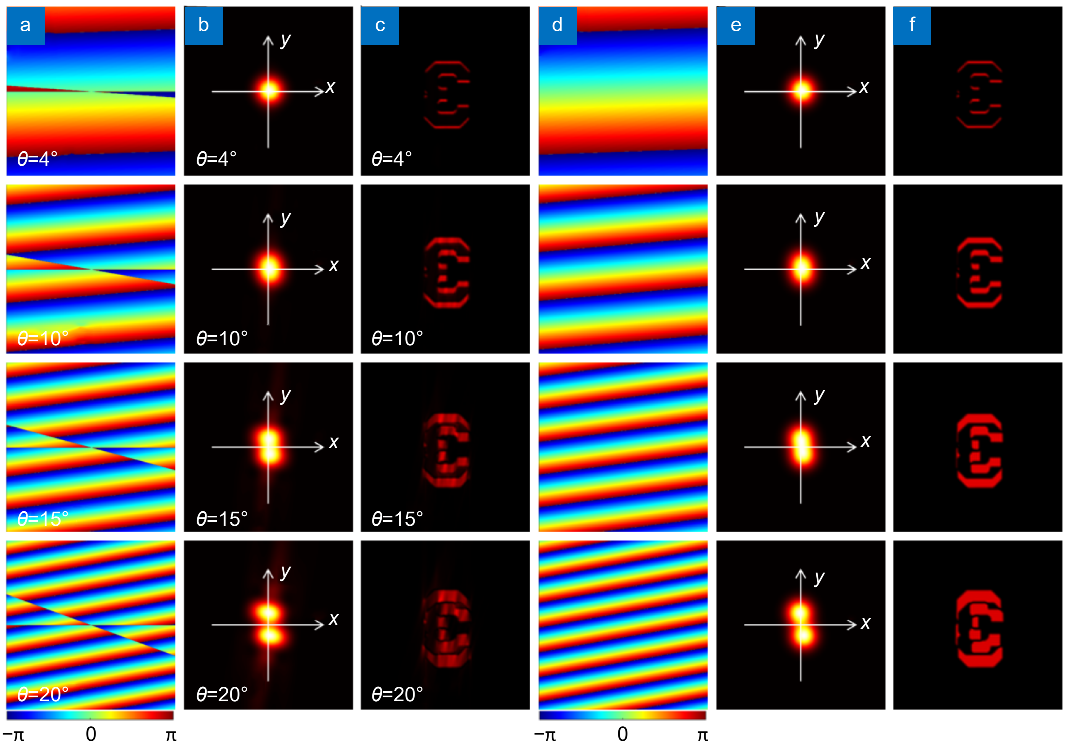

Fig. 7 | Comparison between the gratings generated by the bilayer LC device. (**a**) Theoretical grating phases at different rotation angles *θ*. (**b**, **c**) Corresponding intensity distributions and edge detection results. (**d**) Ideal grating phases calculated using the theoretical model for the corresponding parameters. (**e**, **f**) Corresponding ideal intensity distributions and edge detection results.

synthesized phase generated by the bilayer LC device gradually widen, disrupting the ideal differential formation conditions and consequently leading to a reduction in resolution. The system demonstrates relaxed tolerance to rotational errors (±5°) while demanding high precision in translational alignment (±0.05 mm). Output remains stable within these thresholds, with performance degrading gradually beyond these limits.

Conclusions

In conclusion, we have demonstrated a reconfigurable image processing platform based on diverse structured light modes generated by bilayer LC. The rationale behind this is the programmable manipulation of the composite phase profiles via twisting the layer(s) at in-situ/ex-situ positions. The experimental results for intensity distributions agree well with calculated ones, validating the theoretical modulation model. By leveraging the specific properties of the generated beam modes, we have realized multiple imaging functions, including bright-field imaging, one/two-dimensional edge detection, vertex detection, and resolution-adjustable edge detection. In particular, the variation of the resolution has been quantitatively analyzed. The proposed combination of angular control and spatial offset of the bilayer phase elements provides a new method for tailoring structured beams and implementing mathematical operations, which may pave the avenue for versatile yet economical all-optical data processing. Our future work will focus on the following aspects. Firstly, we will explore alternative design strategies, such as direct imaging schemes that eliminate the need for the 4*f* setup, to promote a more compact footprint. Secondly, to overcome the resolution limit, we plan to integrate our approach with microscopy systems, pushing the capabilities towards super-resolution imaging. This includes employing high-precision alignment and translation stages for improved control and repeatability, alongside refined optical layouts for better beam collimation and the suppression of parasitic reflections and stray light. Finally, we will investigate the application potential of this technology in fields such as biological microscopy and three-dimensional reconstruction.

References

1. Gong L, Zheng W, Ma Y et al. Higher-order coherent anti-Stokes Raman scattering microscopy realizes label-free super-resolution vibrational imaging. *Nat Photonics* **14**, 115–122 (2020).

2. Huo PC, Tan L, Jin YQ et al. Broadband and parallel multiple-order optical spatial differentiation enabled by Bessel vortex modulated metalens. *Nat Commun* **15**, 9045 (2024).
3. Solli DR, Jalali B. Analog optical computing. *Nat Photonics* **9**, 704–706 (2015).
4. Lin X, Rivenson Y, Yardimci NT et al. All-optical machine learning using diffractive deep neural networks. *Science* **361**, 1004–1008 (2018).
5. Zhang T, Zang XF, Tan ZY et al. Integrated polarization, distance, and rotation for multi-DoF diffractive processor and information encryption. *Adv Mater* **37**, 2506222 (2025).
6. Guo ZQ, Tan ZY, Zang XF et al. Polarization-selective unidirectional and bidirectional diffractive neural networks for information security and sharing. *Nat Commun* **16**, 4492 (2025).
7. Tanriover I, Dereshgi SA, Aydin K. Metasurface enabled broadband all optical edge detection in visible frequencies. *Nat Commun* **14**, 6484 (2023).
8. Cotrufo M, Arora A, Singh S et al. Dispersion engineered metasurfaces for broadband, high-NA, high-efficiency, dual-polarization analog image processing. *Nat Commun* **14**, 7078 (2023).
9. Swartz BT, Zheng HY, Forcherio GT et al. Broadband and large-aperture metasurface edge encoders for incoherent infrared radiation. *Sci Adv* **10**, eadk0024 (2024).
10. Qiu XD, Zhang JC, Fan YB et al. Metasurface enabled high-order differentiator. *Nat Commun* **16**, 2437 (2025).
11. Zhu TF, Lou YJ, Zhou YH et al. Generalized spatial differentiation from the spin Hall effect of light and its application in image processing of edge detection. *Phys Rev Appl* **11**, 034043 (2019).
12. Tang P, Li XT, Kim Y et al. Spin Hall effect of light in a dichroic polarizer for multifunctional edge detection. *ACS Photonics* **11**, 4170–4176 (2024).
13. Yang HW, Xie WC, Chen HF et al. Spin-orbit optical broadband achromatic spatial differentiation imaging. *Optica* **11**, 1008–1016 (2024).
14. Fu WW, Zhao D, Li ZQ et al. Ultracompact meta-imagers for arbitrary all-optical convolution. *Light Sci Appl* **11**, 62 (2022).
15. Badloe T, Lee S, Rho J. Computation at the speed of light: metamaterials for all-optical calculations and neural networks. *Adv Photonics* **4**, 064002 (2022).
16. Yu NF, Genevet P, Kats MA et al. Light propagation with phase discontinuities: generalized laws of reflection and refraction. *Science* **334**, 333–337 (2011).
17. Sun SL, He Q, Xiao SY et al. Gradient-index meta-surfaces as a bridge linking propagating waves and surface waves. *Nat Mater* **11**, 426–431 (2012).
18. Yin XB, Ye ZL, Rho J et al. Photonic spin Hall effect at metasurfaces. *Science* **339**, 1405–1407 (2013).
19. Bliokh KY, Rodríguez-Fortuño FJ, Nori F et al. Spin-orbit interactions of light. *Nat Photonics* **9**, 796–808 (2015).
20. Zhao Z, Liu XY, Ji Y et al. Meta-lens digital image correlation. *Opto-Electron Adv* **8**, 250014 (2025).
21. Xu MF, Sang D, Pu MB et al. Time-reversal inverse-designed metasurfaces for on-demand resonance tailoring and dispersion engineering. *Laser Photonics Rev* **19**, 2401819 (2025).
22. Wang B, Rong KX, Maguid E et al. Probing nanoscale fluctuation of ferromagnetic meta-atoms with a stochastic photonic spin Hall effect. *Nat Nanotechnol* **15**, 450–456 (2020).
23. Xie X, Pu MB, Jin JJ et al. Generalized Pancharatnam-Berry phase in rotationally symmetric meta-atoms. *Phys Rev Lett* **126**, 183902 (2021).
24. Silva A, Monticone F, Castaldi G et al. Performing mathematical operations with metamaterials. *Science* **343**, 160–163 (2014).
25. Xu DY, Xu WH, Yang Q et al. All-optical object identification and three-dimensional reconstruction based on optical computing metasurface. *Opto-Electron Adv* **6**, 230120 (2023).
26. You JW, Lan ZH, Panoiu NC. Four-wave mixing of topological edge plasmons in graphene metasurfaces. *Sci Adv* **6**, eaaz3910 (2020).
27. Zeng C, Lu H, Mao D et al. Graphene-empowered dynamic metasurfaces and metadevices. *Opto-Electron Adv* **5**, 200098 (2022).
28. Liu L, Kang L, Mayer TS et al. Hybrid metamaterials for electrically triggered multifunctional control. *Nat Commun* **7**, 13236 (2016).
29. Wang YF, Landreman P, Schoen D et al. Electrical tuning of phase-change antennas and metasurfaces. *Nat Nanotechnol* **16**, 667–672 (2021).
30. Franklin D, Chen Y, Vazquez-Guardado A et al. Polarization-independent actively tunable colour generation on imprinted plasmonic surfaces. *Nat Commun* **6**, 7337 (2015).
31. Franklin D, Frank R, Wu ST et al. Actively addressed single pixel full-colour plasmonic display. *Nat Commun* **8**, 15209 (2017).
32. Kreuzer M, Hanisch F, Eidenschink R et al. Large deuterium isotope effect in the optical nonlinearity of dye-doped liquid crystals. *Phys Rev Lett* **88**, 013902 (2001).
33. Ni YB, Chen C, Wen S et al. Computational spectropolarimetry with a tunable liquid crystal metasurface. *eLight* **2**, 23 (2022).
34. Zhuang XL, Zhang W, Wang KM et al. Active terahertz beam steering based on mechanical deformation of liquid crystal elastomer metasurface. *Light Sci Appl* **12**, 14 (2023).
35. Kang D, Heo H, Yang Y et al. Liquid crystal-integrated metasurfaces for an active photonic platform. *Opto-Electron Adv* **7**, 230216 (2024).
36. Wang GC, Zhou T, Huang JZ et al. Moiré meta-device for flexibly controlled Bessel beam generation. *Photonics Res* **11**, 100–108 (2023).
37. Zhang DP, Zhang F, Pu MB et al. Multi-channel holography via phase-switchable cascaded liquid crystals for optical secret sharing. *Adv Funct Mater* **35**, 2507754 (2025).
38. Chong MZ, Huang SX, Zhang ZK, et al. Reconfigurable terahertz beam splitters enabled by inverse-designed meta-devices. *Photonics Res* **13**, 2328–2338 (2025).
39. Lin QG, Feng F, Zeng XK et al. A universal and versatile terahertz field manipulation mechanism by manipulating near-infrared phases with a dislocation scheme. *Nat Commun* **16**, 6656 (2025).
40. Tian JB, Min L, Chen Y et al. Reconfigurable generation and spin manipulation of structured beams based on cascaded liquid crystal Pancharatnam-Berry phase elements. *Laser Photonics Rev* **19**, 2401378 (2025).
41. Wu XG, Pan K, Wu XY et al. Wavelength-insensitive snapshot Stokes polarimetric imaging based on cascaded metasurfaces. *Adv Photonics* **7**, 016008 (2025).
42. Chen P, Wei BY, Hu W et al. Liquid-crystal-mediated geometric phase: from transmissive to broadband reflective planar optics. *Adv Mater* **32**, 1903665 (2020).
43. Zeng K, Zeng LZ, Yang P et al. Rotational photonic spin Hall effect sensor for liquid chemicals classification via EfficientNet-V2.

ACS Photonics **12**, 485–494 (2025).

44. Zhou JX, Qian HL, Chen CF et al. Optical edge detection based on high-efficiency dielectric metasurface. *Proc Natl Acad Sci USA* **116**, 11137–11140 (2019).
45. Li QY, Liang MG, Liu SQ et al. Phase reconstruction via metasurface-integrated quantum analog operation. *Opto-Electron Adv* **8**, 240239 (2025).
46. Huo PC, Zhang C, Zhu WQ et al. Photonic spin-multiplexing metasurface for switchable spiral phase contrast imaging. *Nano Lett* **20**, 2791–2798 (2020).
47. Yin Y, Yang Y, Li T et al. High-dynamic-resolution optical edge detection based on liquid crystal diffractive moiré lenses with a tunable focal length. *Opt Lett* **46**, 2549–2552 (2021).
48. Wang ZC, Hu GW, Wang XW et al. Single-layer spatial analog meta-processor for imaging processing. *Nat Commun* **13**, 2188 (2022).

Acknowledgements

This work was supported in part by the National Natural Science Foundation of China (12421005, 12374273, and 61805077), in part by the Natural Science Foundation of Hunan Province (2025JJ50046), and in part by the Hunan Provincial Major Sci-Tech Program (2023ZJ1010).

Author contributions

K. Zeng conducted the experimental measurements, prepared the figures, and wrote the first draft of the manuscript. Y. Ke conceived the original idea and supervised the project. Z. Hong contributed to the experiments and figure refinement. L. Zeng directed the theoretical modeling, analyzed the results, and edited the manuscript. X. Zhou coordinated the project administration and provided research resources. All authors have reviewed and approved the final manuscript.

Competing interests

The authors declare no competing financial interests.